

Unrestricted Hartree-Fock Analysis of $\text{Sr}_{3-x}\text{Ca}_x\text{Ru}_2\text{O}_7$

Shigeru Koikegami* , Takashi Yanagisawa¹, and Soh Koike²

Second Lab, LLC, 2-32-1 Umezono, Tsukuba, Ibaraki 305-0045

¹*Electronics and Photonics Research Institute, AIST Tsukuba Central 2, Tsukuba, Ibaraki 305-8568*

²*JSPS, Chiyoda, Tokyo 102-8471*

(Received November 15, 2011)

We investigated the electronic and magnetic structure of $\text{Sr}_{3-x}\text{Ca}_x\text{Ru}_2\text{O}_7$ ($0 \leq x \leq 3$) on the basis of the double-layered three-dimensional multiband Hubbard model with spin-orbit interaction. In our model, lattice distortion is implemented as the modulation of transfer integrals or a crystal field. The most stable states are estimated within the unrestricted Hartree-Fock approximation, in which the collinear spin configurations with five different spin-quantization axes are adopted as candidates. The obtained spin structures for some particular lattice distortions are consistent with the neutron diffraction results for $\text{Ca}_3\text{Ru}_2\text{O}_7$. Also, some magnetic phase transitions can occur due to changes in lattice distortion. These results facilitate the comprehensive understanding of the phase diagram of $\text{Sr}_{3-x}\text{Ca}_x\text{Ru}_2\text{O}_7$.

KEYWORDS: three-dimensional multiband Hubbard model, double-layered ruthenate, lattice distortion, unrestricted Hartree-Fock, spin-orbit interaction

1. Introduction

The series of double-layered ruthenates, $\text{Sr}_{3-x}\text{Ca}_x\text{Ru}_2\text{O}_7$ ($0 \leq x \leq 3$), possesses a variety of phases under a magnetic field (H) or pressure (P). One end-member of the series, $\text{Sr}_3\text{Ru}_2\text{O}_7$, shows the magnetic field-tuned quantum criticality, which is accompanied by the metamagnetic transition around $H \sim 7.85\text{T}$.¹⁾ The metamagnetic transition, which was initially observed by Cao et al.,²⁾ was revealed to be a double transition, and its second transition in the higher-field is sensitive to the field angle.³⁾ Without an applied magnetic field, $\text{Sr}_3\text{Ru}_2\text{O}_7$ behaves as a Fermi liquid at low temperature.⁴⁾ Angle-resolved photo-emission spectroscopy (ARPES) has been used to observe its well-defined Fermi surfaces,⁵⁾ and neutron diffraction methods revealed a lack of that long-range magnetic order.⁶⁾ Meanwhile, inelastic neutron scattering has been used to observe two-dimensional ferromagnetic fluctuations as incommensurate peaks attributed to Fermi surface nesting.⁷⁾ These fluctuations induce ferromagnetism when uniaxial pressures along the c -axis are applied.^{8,9)} Since neutron diffraction analysis displays the temperature and pressure effects on the crystal structure,¹⁰⁾ the phase transition induced by uniaxial pressures suggests that the ferromagnetic fluctuations are susceptible to structural changes. This situation is similar to the ferromagnetic ground state at the surface

*E-mail: shigeami@secondlab.co.jp

of Sr_2RuO_4 , as observed by scanning tunneling microscopy (STM).¹¹⁾ In Sr_2RuO_4 , the ferromagnetic ground state arises due to a perturbative lattice distortion at the surface, that is, an in-plane rotation of the RuO_6 octahedron produced by the surface strain.

Another end-member of the series, $\text{Ca}_3\text{Ru}_2\text{O}_7$, shows two transitions at $T_M = 48\text{K}$ and $T_N = 56\text{K}$.¹²⁾ While T_N has been confirmed as an antiferromagnetic ordering temperature,¹³⁾ T_M was believed to be a Mott-like metal-insulator transition temperature though quantum oscillations in the c -axis resistivity ρ_c , for $H \parallel c$ are observed below T_M .^{14,15)} The electrical resistivity and optical conductivity spectra of single crystals grown by a floating-zone method proved that the ground state of $\text{Ca}_3\text{Ru}_2\text{O}_7$ is quasi-two-dimensional metallic.^{16,17)} Furthermore, the magnetostriction data for the single crystals demonstrated that the first-order transition at T_M can be attributed to a discontinuous change in the lattice constants.¹⁸⁾ The quantum oscillations observed in $\text{Ca}_3\text{Ru}_2\text{O}_7$ have also shown that its ground state is metallic with low-carrier density.¹⁹⁾ The magnetic structure of $\text{Ca}_3\text{Ru}_2\text{O}_7$ in the ground state was clarified using neutron diffraction analysis: the magnetic moments align ferromagnetically within the double layer and antiferromagnetically between the double layers.²⁰⁾ While these magnetic moments lie along the b -axis for $T < T_M$, the first-order transition at T_M changes their directions to align with the a -axis for $T > T_M$.^{21,22)} Moreover, the two transitions at T_N and T_M are respectively weakened by the pressures along the c -axis and those within the ab -plane.²³⁾ These results indicate that the magnetic properties of $\text{Ca}_3\text{Ru}_2\text{O}_7$ are also susceptible to structural changes.

The concentration range $0 < x < 3$ of the $\text{Sr}_{3-x}\text{Ca}_x\text{Ru}_2\text{O}_7$ series has been investigated in addition to the end members.^{24–30)} For the intermediate x of this range, the system exhibits a variety of spin structures: a cluster spin-glass phase for $0.24 \lesssim x \lesssim 1.2$,^{27–29)} and a canted antiferromagnetic phase for $1.2 \lesssim x \lesssim 2.0$.²⁵⁾ By comparing the Weiss temperatures for $H \parallel ab$ with those for $H \parallel c$, Iwata *et al.*²⁸⁾ elucidate that the magnetic easy axis changes continuously from the ab -plane to the c -axis with decreasing x . Peng *et al.*³⁰⁾ confirm that the magnetic easy axis is the b -axis for $x = 2.4$ and $x = 3.0$. This result for $x = 3.0$ is consistent with the result of a neutron diffraction analysis for $\text{Ca}_3\text{Ru}_2\text{O}_7$.²⁰⁾ Moreover, it has been reported that lattice constants vary with x in $\text{Sr}_{3-x}\text{Ca}_x\text{Ru}_2\text{O}_7$.^{28,30)}

$\text{Sr}_{3-x}\text{Ca}_x\text{Ru}_2\text{O}_7$ ($0 \leq x \leq 3$) has also attracted a great deal of theoretical interest. The band structures of its end-members, $\text{Sr}_3\text{Ru}_2\text{O}_7$ and $\text{Ca}_3\text{Ru}_2\text{O}_7$, have been investigated with a local density approximation³¹⁾ or with the local spin density approximation (LSDA).^{32,33)} In particular, the magnetic field-tuned metamagnetic transition of $\text{Sr}_3\text{Ru}_2\text{O}_7$ has been intensively studied as one of the electronic nematic phase transitions on the basis of microscopic theories.^{34–40)} The field-induced orbital-ordered phase of $\text{Ca}_3\text{Ru}_2\text{O}_7$ was also investigated on the basis of the spin/orbital model.⁴¹⁾ However, few theoretical studies have investigated $\text{Sr}_{3-x}\text{Ca}_x\text{Ru}_2\text{O}_7$ ($0 < x < 3$), while a number of theoretical analyses have been performed

for the series of single-layered ruthenates,^{42–49)} $\text{Ca}_{2-x}\text{Sr}_x\text{RuO}_4$ ($0 \leq x \leq 2$), which exhibit the Mott transition at $x \simeq 0.2$.⁵⁰⁾ The two-dimensional multiband Hubbard model has been utilized by these theoretical analyses of the series of single-layered ruthenates. Meanwhile, in order to understand the series of double-layered ruthenates, we need to consider its three-dimensionality. The intrinsic importance of the three-dimensionality can be easily found in the experimental results introduced above (e.g., the magnetic structure of $\text{Ca}_3\text{Ru}_2\text{O}_7$). In this paper, we investigate the electronic and magnetic structures of the double-layered ruthenate $\text{Sr}_{3-x}\text{Ca}_x\text{Ru}_2\text{O}_7$ ($0 \leq x \leq 3$) on the basis of the three-dimensional (3D) multiband Hubbard model. Fully considering possible unequivalent sites and the spin-orbit interaction (SOI), we determine the ground state of our model for each lattice distortion within the unrestricted Hartree-Fock (UHF) approximation. Then, we find that the change in lattice distortion severely affects the electronic and magnetic structures. Our results suggest that the many physical phenomena of $\text{Sr}_{3-x}\text{Ca}_x\text{Ru}_2\text{O}_7$ ($0 \leq x \leq 3$) have a critical relationship with the change in the lattice distortion.

2. Formulation

Our 3D hubbard model with lattice distortion (Fig. 1) consists of A and B sub lattices. We consider every three t_{2g} orbitals of the Ru 4d electrons located in these sublattices on the i -th layer ($i = 1, 2, 3, 4$). Thus, our 3D Hubbard model Hamiltonian, \hat{H} , is composed as follows:

$$\begin{aligned} \hat{H} = & \sum_{i=1}^4 \sum_{j=1}^4 \sum_{\mathbf{k}} \sum_{\sigma} \left[\hat{A}_{i\mathbf{k}\sigma}^\dagger \hat{h}_{ij\mathbf{k}}^{AA} \hat{A}_{j\mathbf{k}\sigma} + \hat{A}_{i\mathbf{k}\sigma}^\dagger \hat{h}_{ij\mathbf{k}}^{AB} \hat{B}_{j\mathbf{k}\sigma} + \hat{B}_{i\mathbf{k}\sigma}^\dagger \hat{h}_{ij\mathbf{k}}^{BA} \hat{A}_{j\mathbf{k}\sigma} + \hat{B}_{i\mathbf{k}\sigma}^\dagger \hat{h}_{ij\mathbf{k}}^{BB} \hat{B}_{j\mathbf{k}\sigma} \right] \\ & + \sum_{i=1}^4 \sum_{\mathbf{k}} \sum_{\sigma\sigma'} \left[\hat{A}_{i\mathbf{k}\sigma}^\dagger \hat{l}_{\sigma\sigma'}^A \hat{A}_{i\mathbf{k}\sigma'} + \hat{B}_{i\mathbf{k}\sigma}^\dagger \hat{l}_{\sigma\sigma'}^B \hat{B}_{i\mathbf{k}\sigma'} \right] \\ & + \hat{H}' - \mu \sum_{i=1}^4 \sum_{\mathbf{k}} \sum_{\sigma} \left[\hat{A}_{i\mathbf{k}\sigma}^\dagger \hat{A}_{i\mathbf{k}\sigma} + \hat{B}_{i\mathbf{k}\sigma}^\dagger \hat{B}_{i\mathbf{k}\sigma} \right]. \end{aligned} \quad (1)$$

Here we use the abbreviations $\hat{A}_{i\mathbf{k}\sigma}^\dagger \equiv \left(A_{i\mathbf{k}\sigma}^{yz\dagger} A_{i\mathbf{k}\sigma}^{zx\dagger} A_{i\mathbf{k}\sigma}^{xy\dagger} \right)$, $\hat{A}_{i\mathbf{k}\sigma} \equiv {}^t(A_{i\mathbf{k}\sigma}^{yz} A_{i\mathbf{k}\sigma}^{zx} A_{i\mathbf{k}\sigma}^{xy})$, $\hat{B}_{i\mathbf{k}\sigma}^\dagger \equiv \left(B_{i\mathbf{k}\sigma}^{yz\dagger} B_{i\mathbf{k}\sigma}^{zx\dagger} B_{i\mathbf{k}\sigma}^{xy\dagger} \right)$, and $\hat{B}_{i\mathbf{k}\sigma} \equiv {}^t(B_{i\mathbf{k}\sigma}^{yz} B_{i\mathbf{k}\sigma}^{zx} B_{i\mathbf{k}\sigma}^{xy})$, where $A_{i\mathbf{k}\sigma}^\varphi$ ($A_{i\mathbf{k}\sigma}^{\varphi\dagger}$) and $B_{i\mathbf{k}\sigma}^\varphi$ ($B_{i\mathbf{k}\sigma}^{\varphi\dagger}$) are the annihilation (creation) operators for the electron in the A and B sublattice on the i -th layer ($i = 1, 2, 3, 4$), as specified by orbital $\varphi = \{yz, zx, xy\}$, momentum \mathbf{k} , and spin $\sigma = \{\uparrow, \downarrow\}$, respectively. μ is the chemical potential. The nonvanishing $\hat{h}_{ij\mathbf{k}}^{AA}$, $\hat{h}_{ij\mathbf{k}}^{AB}$, $\hat{h}_{ij\mathbf{k}}^{BA}$, and $\hat{h}_{ij\mathbf{k}}^{BB}$ in eq. (1) are

$$\hat{h}_{ii\mathbf{k}}^{AA} = \hat{h}_{ii\mathbf{k}}^{BB} = \begin{pmatrix} 0 & \lambda_{\mathbf{k}} & 0 \\ \lambda_{\mathbf{k}} & 0 & 0 \\ 0 & 0 & \epsilon_{\mathbf{k}} \end{pmatrix} \quad (i = 1, 2, 3, 4), \quad (2)$$

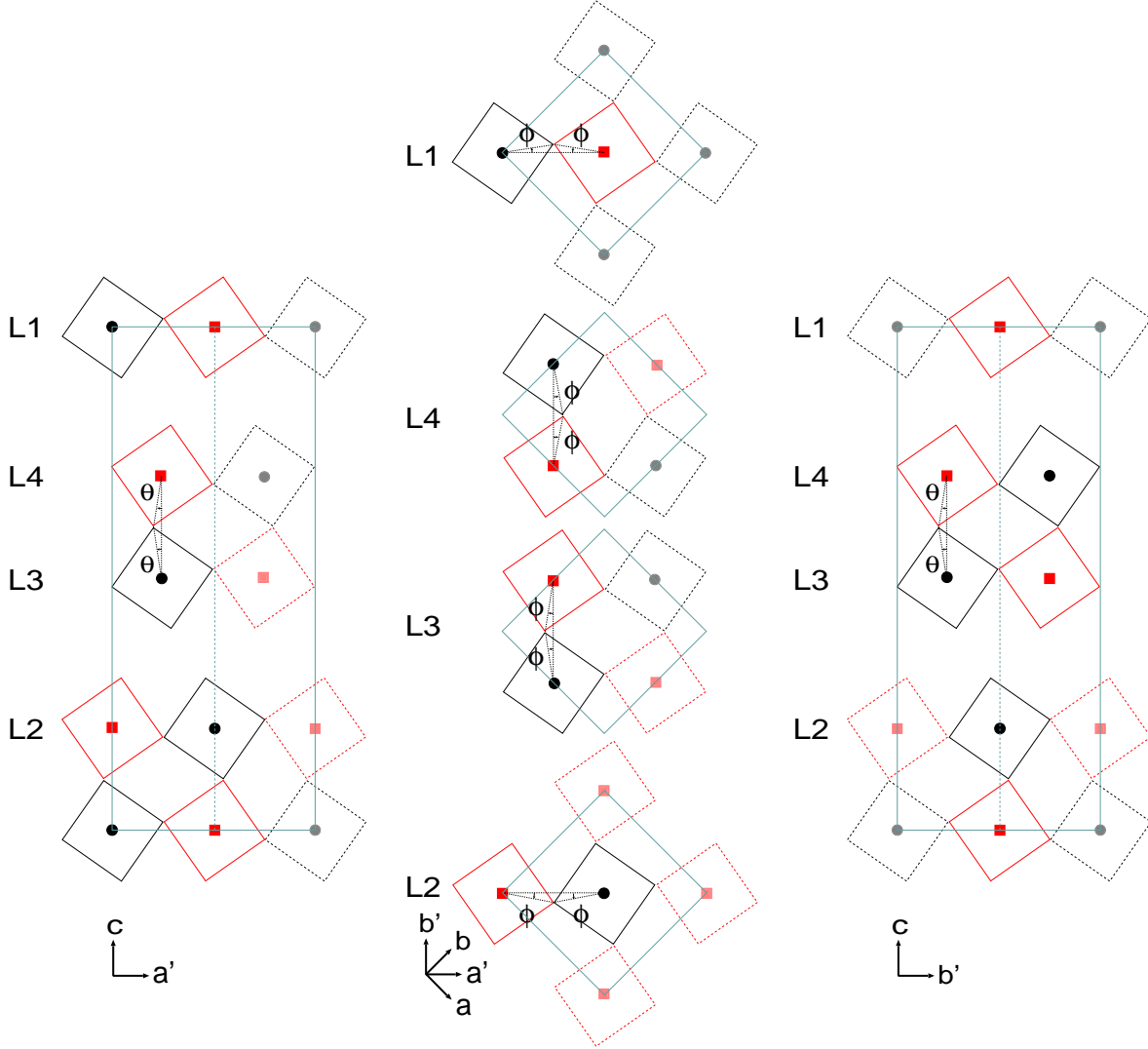


Fig. 1. (Color online) Unit cell of our 3D Hubbard model: (left) projection onto the $a'c$ -plane, (center) projection onto the $a'b'(ab)$ -plane, and (right) projection onto the $b'c$ -plane. The diamonds with solid circles(squares) represent the RuO_6 octahedrons on the A(B) sublattice. The Ru sites in these octahedrons are indicated by solid circles. L_i indicates the i -th layer ($i = 1, 2, 3, 4$). ϕ and θ represent the rotation and tilting angles of the RuO_6 octahedron, respectively.

$$\hat{h}_{ii\mathbf{k}}^{AB} = \hat{h}_{ii\mathbf{k}}^{BA} = \begin{pmatrix} t_{\mathbf{k}}^{yz} & 0 & 0 \\ 0 & t_{\mathbf{k}}^{zx} & 0 \\ 0 & 0 & t_{\mathbf{k}}^{xy} \end{pmatrix} \quad (i = 1, 2, 3, 4), \quad (3)$$

$$\hat{h}_{12\mathbf{k}}^{AB} = \hat{h}_{12\mathbf{k}}^{BA} = [\hat{h}_{21\mathbf{k}}^{AB}]^* = [\hat{h}_{21\mathbf{k}}^{BA}]^* = \hat{h}_{34\mathbf{k}}^{AB} = \hat{h}_{34\mathbf{k}}^{BA} = [\hat{h}_{43\mathbf{k}}^{AB}]^* = [\hat{h}_{43\mathbf{k}}^{BA}]^* = \begin{pmatrix} c_{\mathbf{k}}^z & 0 & 0 \\ 0 & c_{\mathbf{k}}^z & 0 \\ 0 & 0 & 0 \end{pmatrix}, \quad (4)$$

$$\hat{h}_{32\mathbf{k}}^{AA} = \hat{h}_{32\mathbf{k}}^{BB} = [\hat{h}_{23\mathbf{k}}^{AA}]^* = [\hat{h}_{23\mathbf{k}}^{BB}]^* = \hat{h}_{14\mathbf{k}}^{AA} = \hat{h}_{14\mathbf{k}}^{BB} = [\hat{h}_{41\mathbf{k}}^{AA}]^* = [\hat{h}_{41\mathbf{k}}^{BB}]^* = \begin{pmatrix} c_{\mathbf{k}}^y & 0 & 0 \\ 0 & c_{\mathbf{k}}^y & 0 \\ 0 & 0 & 0 \end{pmatrix}, \quad (5)$$

and

$$\hat{h}_{32\mathbf{k}}^{AB} = \hat{h}_{32\mathbf{k}}^{BA} = [\hat{h}_{23\mathbf{k}}^{AB}]^* = [\hat{h}_{23\mathbf{k}}^{BA}]^* = \hat{h}_{14\mathbf{k}}^{AB} = \hat{h}_{14\mathbf{k}}^{BA} = [\hat{h}_{41\mathbf{k}}^{AB}]^* = [\hat{h}_{41\mathbf{k}}^{BA}]^* = \begin{pmatrix} c_{\mathbf{k}}^x & 0 & 0 \\ 0 & c_{\mathbf{k}}^x & 0 \\ 0 & 0 & 0 \end{pmatrix}, \quad (6)$$

where we use the abbreviations

$$c_{\mathbf{k}}^x = -2t'_{\perp} e^{i(3k_z/10)} \cos \frac{k_x}{2}, \quad (7)$$

$$c_{\mathbf{k}}^y = -2t'_{\perp} e^{i(3k_z/10)} \cos \frac{k_y}{2}, \quad (8)$$

$$c_{\mathbf{k}}^z = -t_{\perp} (\cos \phi \cos 2\theta)^2 e^{-i(k_z/5)}, \quad (9)$$

$$t_{\mathbf{k}}^{xy} = -2t_1 (\cos 2\phi \cos \theta)^2 \left[\cos \frac{k_x + k_y}{2} + \cos \frac{k_x - k_y}{2} \right], \quad (10)$$

$$t_{\mathbf{k}}^{yz} = -2t_4 \cos \frac{k_x + k_y}{2} - 2t_3 (\cos \phi \cos 2\theta)^2 \cos \frac{k_x - k_y}{2}, \quad (11)$$

$$t_{\mathbf{k}}^{zx} = -2t_3 (\cos \phi \cos 2\theta)^2 \cos \frac{k_x + k_y}{2} - 2t_4 \cos \frac{k_x - k_y}{2}, \quad (12)$$

$$\epsilon_{\mathbf{k}} = -2t_2 (\cos k_x + \cos k_y) - \Delta, \quad (13)$$

and

$$\lambda_{\mathbf{k}} = 2\lambda_0 (\cos k_x - \cos k_y). \quad (14)$$

In eqs. (7)–(9) t_{\perp} and t'_{\perp} represent inter-layer transfers, and in eqs. (10)–(14), t_1 , t_2 , t_3 , t_4 , and λ_0 represent intra-layer transfers. Δ in eq. (13) represents the energy level difference between the d_{xy} and $d_{yz}(d_{zx})$ orbitals due to the crystal field. The terms $\hat{l}_{\sigma\sigma'}^A$ and $\hat{l}_{\sigma\sigma'}^B$ in eq. (1), arising from the spin-orbit interaction, are determined from formulas that depend on the choice of the spin-quantization axis. Here we only consider collinear spin states, with the five different spin-quantization axes as candidates for the most stable states. These five are the c -, a' -, b' -, a -, and b -axes. When we consider the state with the spin-quantization axis parallel to the c -axis, we represent $\hat{l}_{\sigma\sigma'}^A$ and $\hat{l}_{\sigma\sigma'}^B$ by $\hat{l}_{\sigma\sigma'}^{A(c)}$ and $\hat{l}_{\sigma\sigma'}^{B(c)}$, respectively. These are defined as follows:

$$\hat{l}_{\uparrow\uparrow}^{A(c)} = -\hat{l}_{\downarrow\downarrow}^{A(c)} = \hat{l}_{\uparrow\uparrow}^{B(c)} = -\hat{l}_{\downarrow\downarrow}^{B(c)} = \begin{pmatrix} 0 & \frac{i}{2}\zeta & 0 \\ -\frac{i}{2}\zeta & 0 & 0 \\ 0 & 0 & 0 \end{pmatrix} \quad (15)$$

and

$$\hat{l}_{\uparrow\downarrow}^{A(c)} = -[\hat{l}_{\downarrow\uparrow}^{A(c)}]^* = \hat{l}_{\uparrow\downarrow}^{B(c)} = -[\hat{l}_{\downarrow\uparrow}^{B(c)}]^* = \begin{pmatrix} 0 & 0 & -\frac{1}{2}\zeta \\ 0 & 0 & \frac{i}{2}\zeta \\ \frac{1}{2}\zeta & -\frac{i}{2}\zeta & 0 \end{pmatrix}. \quad (16)$$

Similarly, when we consider the state with the spin-quantization axis parallel to the a' -axis, we have

$$\hat{l}_{\uparrow\uparrow}^{A(a')} = -\hat{l}_{\downarrow\downarrow}^{A(a')} = \hat{l}_{\uparrow\uparrow}^{B(a')} = -\hat{l}_{\downarrow\downarrow}^{B(a')} = \cos\phi \begin{pmatrix} 0 & 0 & 0 \\ 0 & 0 & \frac{i}{2}\zeta \\ 0 & -\frac{i}{2}\zeta & 0 \end{pmatrix} \quad (17)$$

and

$$\hat{l}_{\uparrow\downarrow}^{A(a')} = -[\hat{l}_{\downarrow\uparrow}^{A(a')}]^* = \hat{l}_{\uparrow\downarrow}^{B(a')} = -[\hat{l}_{\downarrow\uparrow}^{B(a')}]^* = \cos\phi \begin{pmatrix} 0 & \frac{1}{2}\zeta & -\frac{i}{2}\zeta \\ -\frac{1}{2}\zeta & 0 & 0 \\ \frac{i}{2}\zeta & 0 & 0 \end{pmatrix}, \quad (18)$$

and when we consider the state with the spin-quantization axis parallel to the b' -axis, we have

$$\hat{l}_{\uparrow\uparrow}^{A(b')} = -\hat{l}_{\downarrow\downarrow}^{A(b')} = \hat{l}_{\uparrow\uparrow}^{B(b')} = -\hat{l}_{\downarrow\downarrow}^{B(b')} = \cos\phi \begin{pmatrix} 0 & 0 & -\frac{i}{2}\zeta \\ 0 & 0 & 0 \\ \frac{i}{2}\zeta & 0 & 0 \end{pmatrix} \quad (19)$$

and

$$\hat{l}_{\uparrow\downarrow}^{A(b')} = -[\hat{l}_{\downarrow\uparrow}^{A(b')}]^* = \hat{l}_{\uparrow\downarrow}^{B(b')} = -[\hat{l}_{\downarrow\uparrow}^{B(b')}]^* = \cos\phi \begin{pmatrix} 0 & \frac{i}{2}\zeta & 0 \\ -\frac{i}{2}\zeta & 0 & \frac{1}{2}\zeta \\ 0 & -\frac{1}{2}\zeta & 0 \end{pmatrix}. \quad (20)$$

Furthermore, when we consider the state with the spin-quantization axis parallel to the a -axis, we have

$$\hat{l}_{\sigma\sigma'}^{A(a)} = -\frac{1}{\sqrt{2}}(1 + \tan\phi)\hat{l}_{\sigma\sigma'}^{A(a')} + \frac{1}{\sqrt{2}}(1 - \tan\phi)\hat{l}_{\sigma\sigma'}^{A(b')} \quad (21)$$

and

$$\hat{l}_{\sigma\sigma'}^{B(a)} = -\frac{1}{\sqrt{2}}(1 - \tan\phi)\hat{l}_{\sigma\sigma'}^{B(a')} + \frac{1}{\sqrt{2}}(1 + \tan\phi)\hat{l}_{\sigma\sigma'}^{B(b')}, \quad (22)$$

using eqs. (17)- (20). Here we ignore their θ -dependencies. Similarly, when we consider the state with the spin-quantization axis parallel to the b -axis, we have

$$\hat{l}_{\sigma\sigma'}^{A(b)} = \frac{1}{\sqrt{2}}(1 + \tan\phi)\hat{l}_{\sigma\sigma'}^{A(a')} + \frac{1}{\sqrt{2}}(1 - \tan\phi)\hat{l}_{\sigma\sigma'}^{A(b')} \quad (23)$$

and

$$\hat{l}_{\sigma\sigma'}^{B(b)} = \frac{1}{\sqrt{2}}(1 - \tan\phi)\hat{l}_{\sigma\sigma'}^{B(a')} + \frac{1}{\sqrt{2}}(1 + \tan\phi)\hat{l}_{\sigma\sigma'}^{B(b')}. \quad (24)$$

The interacting part \hat{H}' in eq. (1) is represented by

$$\begin{aligned}
\hat{H}' = & \frac{U}{2N} \sum_{i=1}^4 \sum_{\mathbf{k}\mathbf{k}'\mathbf{q}} \sum_{\varphi} \sum_{\sigma} \left[A_{i\mathbf{k}+\mathbf{q}\sigma}^{\varphi\dagger} A_{i\mathbf{k}'-\mathbf{q}-\sigma}^{\varphi\dagger} A_{i\mathbf{k}'-\sigma}^{\varphi} A_{i\mathbf{k}\sigma}^{\varphi} + B_{i\mathbf{k}+\mathbf{q}\sigma}^{\varphi\dagger} B_{i\mathbf{k}'-\mathbf{q}-\sigma}^{\varphi\dagger} B_{i\mathbf{k}'-\sigma}^{\varphi} B_{i\mathbf{k}\sigma}^{\varphi} \right] \\
& + \frac{V}{2N} \sum_{i=1}^4 \sum_{\mathbf{k}\mathbf{k}'\mathbf{q}} \sum_{\varphi} \sum_{\varphi' \neq \varphi} \sum_{\sigma\sigma'} \left[A_{i\mathbf{k}+\mathbf{q}\sigma}^{\varphi\dagger} A_{i\mathbf{k}'-\mathbf{q}\sigma'}^{\varphi'\dagger} A_{i\mathbf{k}'\sigma'}^{\varphi'} A_{i\mathbf{k}\sigma}^{\varphi} + B_{i\mathbf{k}+\mathbf{q}\sigma}^{\varphi\dagger} B_{i\mathbf{k}'-\mathbf{q}\sigma'}^{\varphi'\dagger} B_{i\mathbf{k}'\sigma'}^{\varphi'} B_{i\mathbf{k}\sigma}^{\varphi} \right] \\
& + \frac{J}{2N} \sum_{i=1}^4 \sum_{\mathbf{k}\mathbf{k}'\mathbf{q}} \sum_{\varphi} \sum_{\varphi' \neq \varphi} \sum_{\sigma\sigma'} \left[A_{i\mathbf{k}+\mathbf{q}\sigma}^{\varphi\dagger} A_{i\mathbf{k}'-\mathbf{q}\sigma'}^{\varphi'\dagger} A_{i\mathbf{k}'\sigma'}^{\varphi} A_{i\mathbf{k}\sigma}^{\varphi'} + B_{i\mathbf{k}+\mathbf{q}\sigma}^{\varphi\dagger} B_{i\mathbf{k}'-\mathbf{q}\sigma'}^{\varphi'\dagger} B_{i\mathbf{k}'\sigma'}^{\varphi} B_{i\mathbf{k}\sigma}^{\varphi'} \right],
\end{aligned} \tag{25}$$

where N is the number of \mathbf{k} -space points in the first Brillouin zone (FBZ). Here we only consider the on-site interactions, i.e. Coulomb repulsion in the same orbital U , Coulomb repulsion in different orbitals V , and the exchange interaction J . We adopt the UHF approximation with respect to every two sublattices, four layers, three orbitals and two spin states. Thus, we define

$$\frac{1}{N} \left\langle A_{i\mathbf{k}\sigma}^{\varphi\dagger} A_{i\mathbf{k}'\sigma'}^{\varphi'} \right\rangle \equiv n_{i\varphi\sigma}^A \delta_{\mathbf{k}\mathbf{k}'} \delta_{\varphi\varphi'} \delta_{\sigma\sigma'} \tag{26}$$

and

$$\frac{1}{N} \left\langle B_{i\mathbf{k}\sigma}^{\varphi\dagger} B_{i\mathbf{k}'\sigma'}^{\varphi'} \right\rangle \equiv n_{i\varphi\sigma}^B \delta_{\mathbf{k}\mathbf{k}'} \delta_{\varphi\varphi'} \delta_{\sigma\sigma'}. \tag{27}$$

Then, we can approximate \hat{H}' as follows:

$$\begin{aligned}
\hat{H}' \approx & \sum_{i=1}^4 \sum_{\varphi} \sum_{\sigma} \left[\left\{ U n_{i\varphi-\sigma}^A + \sum_{\varphi' \neq \varphi} \left(V \sum_{\sigma'} n_{i\varphi'\sigma'}^A - J n_{i\varphi'\sigma}^A \right) \right\} \left(\sum_{\mathbf{k}} A_{i\mathbf{k}\sigma}^{\varphi\dagger} A_{i\mathbf{k}\sigma}^{\varphi} - \frac{N}{2} n_{i\varphi\sigma}^A \right) \right. \\
& \left. + \left\{ U n_{i\varphi-\sigma}^B + \sum_{\varphi' \neq \varphi} \left(V \sum_{\sigma'} n_{i\varphi'\sigma'}^B - J n_{i\varphi'\sigma}^B \right) \right\} \left(\sum_{\mathbf{k}} B_{i\mathbf{k}\sigma}^{\varphi\dagger} B_{i\mathbf{k}\sigma}^{\varphi} - \frac{N}{2} n_{i\varphi\sigma}^B \right) \right]
\end{aligned} \tag{28}$$

In order to determine the most stable of the five candidates, we conduct a self-consistent calculation for each candidate and find the one with the lowest electronic energy as estimated by eqs. (1) and (28). Hence, we can translate the most stable spin-quantization axis as the magnetic easy axis. Moreover, for the electronic state that we determine has the most stable spin-quantization axis, we can calculate the five types of the magnetic order parameters. Four of these types are antiferromagnetic order parameters, referred to as A₁-AFM, A₂-AFM, C₁-AFM, and C₂-AFM and expressed as

$$m(\text{A}_1) = \left| \sum_{i=1}^2 (m_i^A + m_i^B) - \sum_{i=3}^4 (m_i^A + m_i^B) \right|, \tag{29}$$

t_1	t_2	t_3	t_4	t_\perp	t'_\perp	λ_0	Δ	ζ	U	V	J	
0.40	0.08	0.40	0.04	0.24	0.04	0.04	0.00	0.16	0.80	0.40	0.20	Fig. 2
0.40	0.08	0.40	0.04	0.24	0.04	0.04	0.16	0.16	0.80	0.40	0.20	Fig. 3
0.40	0.08	0.40	0.04	0.24	0.04	0.04	0.00	0.16	1.00	0.50	0.25	Fig. 4
0.40	0.08	0.40	0.04	0.24	0.04	0.04	0.16	0.16	1.00	0.50	0.25	Fig. 5

Table I. The parameter sets for the calculations. The parameter unit is eV.

$$m(A_2) = \left| \sum_{i=2}^3 (m_i^A + m_i^B) - \sum_{i=4}^1 (m_i^A + m_i^B) \right|, \quad (30)$$

$$m(C_1) = \left| \sum_{i=1}^4 (-1)^i (m_i^A - m_i^B) \right|, \quad (31)$$

$$m(C_2) = \left| \sum_{i=2}^3 (m_i^A - m_i^B) - \sum_{i=4}^1 (m_i^A - m_i^B) \right|, \quad (32)$$

respectively. The fifth type is the ferromagnetic order parameter, expressed as

$$m(\text{FM}) = \left| \sum_{i=1}^4 (m_i^A + m_i^B) \right|. \quad (33)$$

Here, we introduce the magnetic momentum on each site:

$$m_i^{A(B)} \equiv \frac{1}{2} \sum_{\varphi} \left[n_{i\varphi\uparrow}^{A(B)} - n_{i\varphi\downarrow}^{A(B)} \right]. \quad (34)$$

Then we determine the magnetic order with the largest magnitude of these five order parameters for each parameter set.

3. Results and Discussion

In our numerical calculations, we divide FBZ into a $20 \times 20 \times 20$ equally spaced meshes. The parameter sets in eqs. (7)–(20) and (25) for these calculations are selected as shown in Table I. The choice of these parameters is based on preceding theoretical works.³⁹⁾ The ratios V/U and J/U in each set are fixed at 0.5 and 0.25, respectively. For each set in Table I, both the rotation angle ϕ and the tilting angle θ are varied from 0° to 20° by 5° . All resulting self-consistent fields $n_{i\varphi\sigma}^A$ and $n_{i\varphi\sigma}^B$ have four digits of accuracy, and they satisfy

$$\sum_{i=1}^4 \sum_{\varphi} \sum_{\sigma} (n_{i\varphi\sigma}^A + n_{i\varphi\sigma}^B) = 32, \quad (35)$$

which means that there are four electrons per Ru site.

We summarize our numerical results, as indicated by the last column of Table I, in Figs. 2–5. The figures show the magnetic easy axis, magnetic phase, and density of states (DOS's) determined for each pair of (ϕ, θ) . Here, the magnetic phase is defined as the paramagnetism (PM) when none of the order parameters reach a finite value, and the magnetic phase is

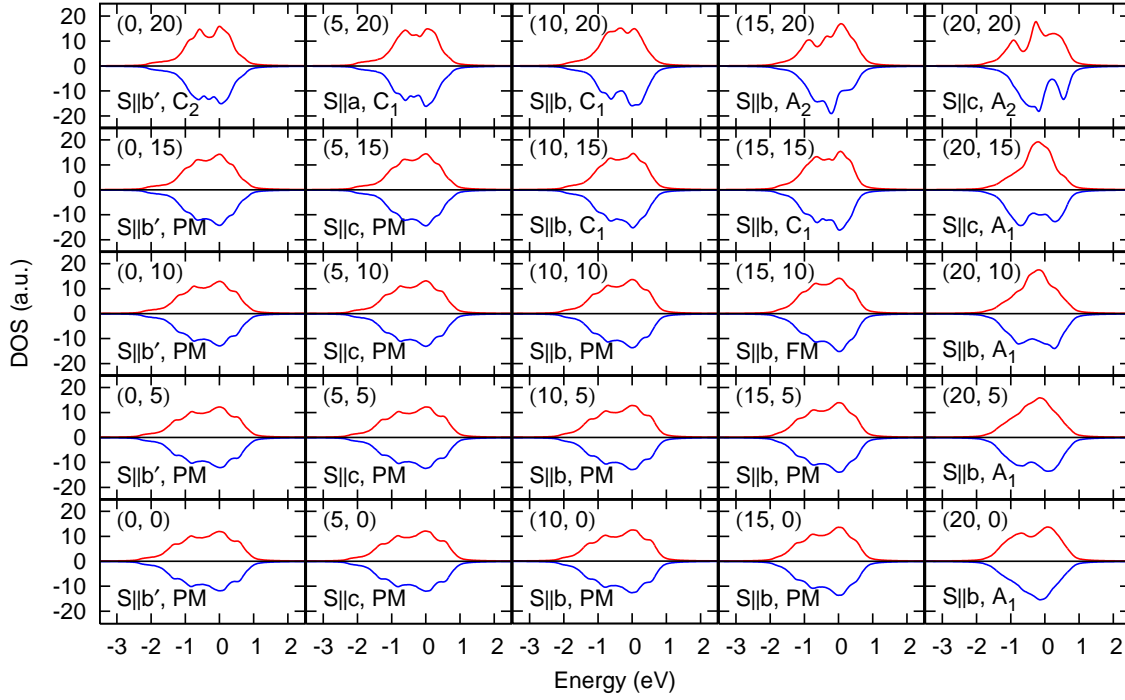


Fig. 2. (Color online) The magnetic easy axis, magnetic phase, and density of states (DOS) determined when $\Delta = 0.00$ eV and $U = 0.8$ eV. The unit of each (ϕ, θ) is provided in $^\circ$ (degrees). Positive DOS is for spin up and negative DOS is for spin down.

defined as X when several order parameters simultaneously reach the maximum value of the five. We can easily recognize that the various magnetic phases appear and that their phase transition is caused by the fractional change of the lattice distortion. The magnetic easy axis can vary even in the same magnetic phase. The variations in the magnetic phase and easy axis are caused by the transfers and SOI, which both depend on the lattice distortion. While the SOI dependence on the lattice distortion plays the primary role in the determination of the magnetic easy axis, the transfers dependence is more responsible for determining the magnetic phase.

The energy level difference between d_{xy} and $d_{yz}(d_{zx})$, i.e. Δ , also affects the electronic states since it relatively lowers the bands from the d_{xy} orbital as well as enhances the full bandwidth W . When we compare Fig. 2 with Fig. 3, or Fig. 4 with Fig. 5, we find that a positive Δ makes the PM phase stable for a wider range of lattice distortion parameters. This can be derived from the decrease in U/W in conjunction with the change in Δ . In $\text{Ca}_3\text{Ru}_2\text{O}_7$, the lattice constants abruptly change at $T_M = 48\text{K}$, where the first-order transition occurs^{14,18)} due to Jahn-Teller distortions of the RuO_6 octahedra.¹⁴⁾ Thus, we can naturally assign our

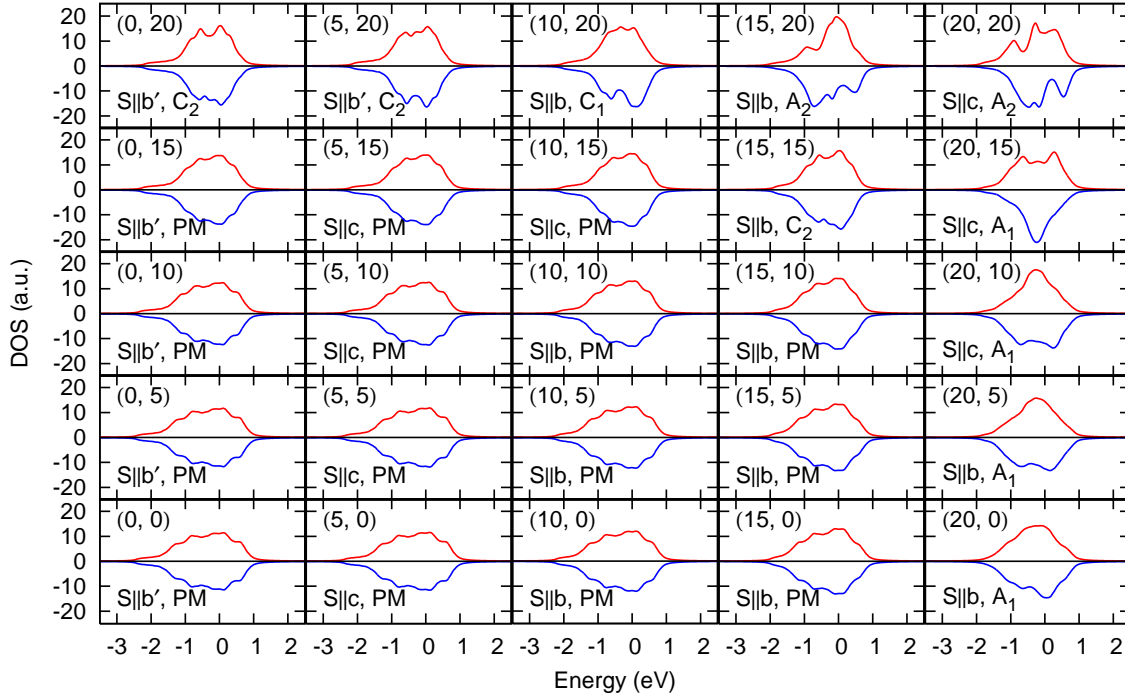


Fig. 3. (Color online) The magnetic easy axis, magnetic phase, and DOS determined when $\Delta = 0.16$ eV and $U = 0.8$ eV.

results for $\Delta > 0$ (Figs. 3 and 5) to the quasi-two-dimensional metallic state of $\text{Ca}_3\text{Ru}_2\text{O}_7$ for $T < T_M$.^{16,17)}

In our model, all bands can be categorized into two types: bands derived from the d_{xy} orbital or bands derived from the $d_{yz}(d_{zx})$ orbital. When we respectively define their bandwidths as W_{xy} and $W_{yz,zx}$, their dependence on ϕ and θ is like $W_{xy} \propto (\cos 2\phi \cos \theta)^2$ and $W_{yz,zx} \propto (\cos \phi \cos 2\theta)^2$, due to eqs. (10)-(12). When either the rotation (ϕ) or the tilting (θ) increases, both W_{xy} and $W_{yz,zx}$ decrease and U/W increases. Thus, the lattice distortion prefers the AFM phase rather than the PM phase due to a large U/W , as shown in Figs. 2 and 3. Moreover, each bandwidth dependence creates differences in the lattice distortion effects on the electronic state between ϕ and θ . The results for $(\phi, \theta) = (20, 0)$ and $(\phi, \theta) = (0, 20)$ in Figs. 2 and 3 provide clear evidence of these differences.

Figs. 6 and 7 show the obtained antiferromagnetic structures. In these structures, A_1 -AFM along the b -axis is consistent with the structure of $\text{Ca}_3\text{Ru}_2\text{O}_7$ observed by a neutron diffraction analysis.²⁰⁾ The A_1 -AFM phase appears as shown in Figs. 2-3. This phase has been proved to be the most stable state by Singh and Auluck in the LSDA for $\text{Ca}_3\text{Ru}_2\text{O}_7$, where it was noted as AF1.³³⁾

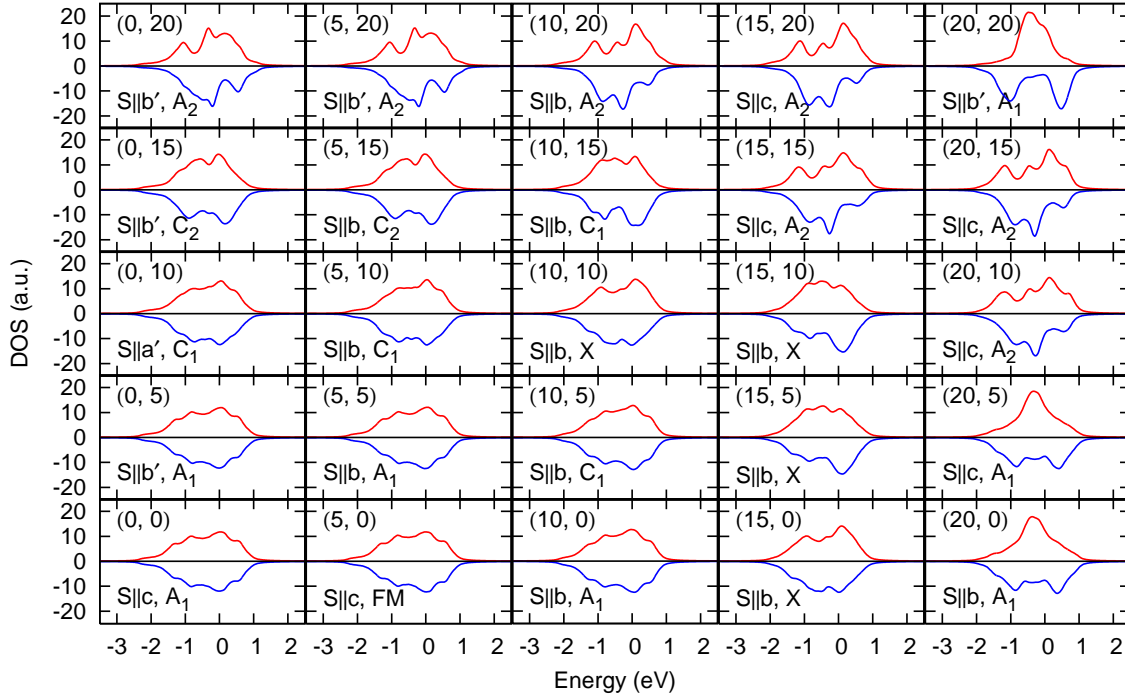


Fig. 4. (Color online) The magnetic easy axis, magnetic phase, and DOS determined when $\Delta = 0.00$ eV and $U = 1.0$ eV.

The FM phase sometimes appears in the neighborhood of the A_1 -AFM phase as shown in Figs. 2 and 4. In the A_1 -AFM phase, the magnetic moments align ferromagnetically within the double layer, and the ferromagnetic correlation within this double layer is stronger than the antiferromagnetic correlation; this has been confirmed by an inelastic neutron scattering study for the spin-wave excitation in $\text{Ca}_3\text{Ru}_2\text{O}_7$.⁵¹⁾ In the intermediate regime where the AFM correlation between the double layer is not fully developed, electrons show the FM order as a whole although their magnetic moments are small. Thus, FM can be derived from the perturbative change of lattice distortion in our model, and this supports the emergence of FM induced by uniaxial pressures along the c -axis in $\text{Sr}_3\text{Ru}_2\text{O}_7$.^{8,9)}

Let us note that the X magnetic phase appears in Figs. 4 and 5. Several spin configurations have almost the equivalent energy in this phase, so that the energy profile of this phase has a multi-valley structure in its ground state. Thus, we can identify the X magnetic phase as a cluster spin-glass phase in $\text{Sr}_{3-x}\text{Ca}_x\text{Ru}_2\text{O}_7$ for $0.24 \lesssim x \lesssim 1.2$.²⁷⁻²⁹⁾ The variation of x in $\text{Sr}_{3-x}\text{Ca}_x\text{Ru}_2\text{O}_7$ is accompanied by the change in lattice distortion,^{28,30)} which must be one reason why the electronic state changes with x unless the carrier density remains the same.

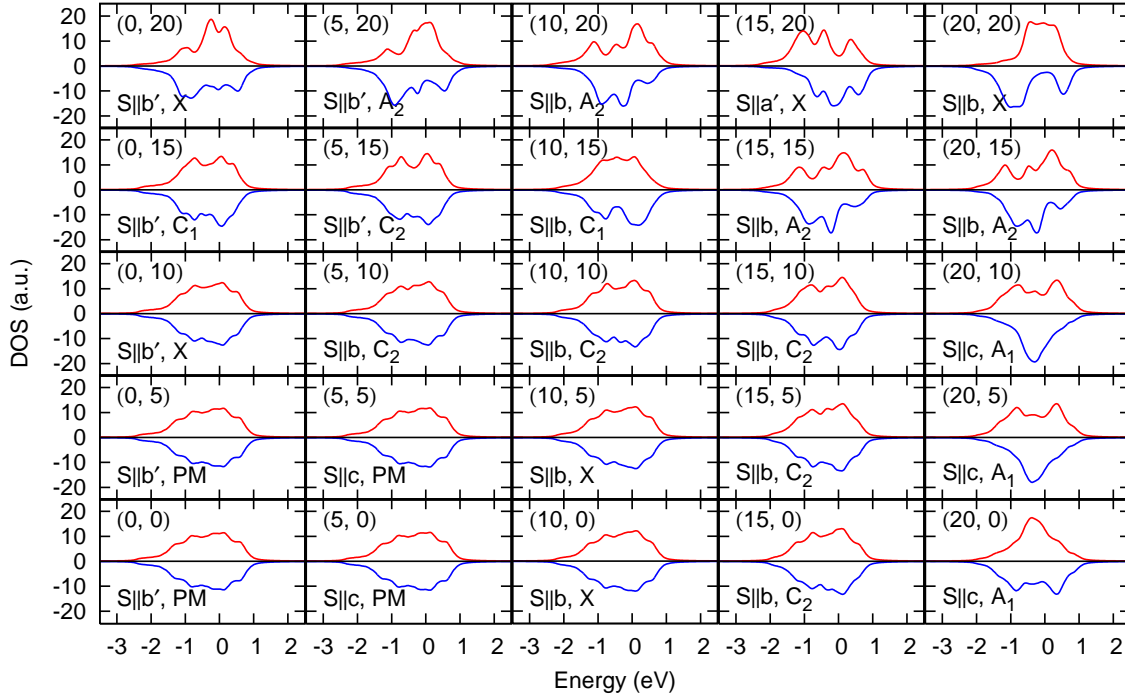


Fig. 5. (Color online) The magnetic easy axis, magnetic phase, and DOS determined when $\Delta = 0.16$ eV and $U = 1.0$ eV.

4. Conclusion

In this paper, we examined the lattice distortion effects on $\text{Sr}_{3-x}\text{Ca}_x\text{Ru}_2\text{O}_7$ using the double-layered 3D multiband Hubbard model with SOI by the unrestricted Hartree-Fock calculation. For some types of lattice distortion, we obtained the A_1 -AFM phase along the b -axis, consistent with the neutron scattering result for $\text{Ca}_3\text{Ru}_2\text{O}_7$. Our results also indicate a possible ferromagnetic transition which is susceptible to the change in lattice distortion and the existence of a cluster spin-glass phase for the intermediate x . The electronic states with these above results are all metallic. This suggests that a number of physical phenomena in zero-field can be explained without the existence of a metal-insulator transition. In a recent experiment it was reported that the field-induced metamagnetic transition drives small lattice distortion in $\text{Sr}_3\text{Ru}_2\text{O}_7$.⁵²⁾ To elucidate such a relation between lattice distortion and quantum critical phenomena, the study of the lattice distortion effects on $\text{Sr}_{3-x}\text{Ca}_x\text{Ru}_2\text{O}_7$ in a finite magnetic field is needed in the future.

Acknowledgments

The authors are grateful to Drs. Y. Yoshida, S.-I. Ikeda, I. Hase, N. Shirakawa, K. Iwata, and S. Kouno for their fruitful discussions. The early stage of our computational study has

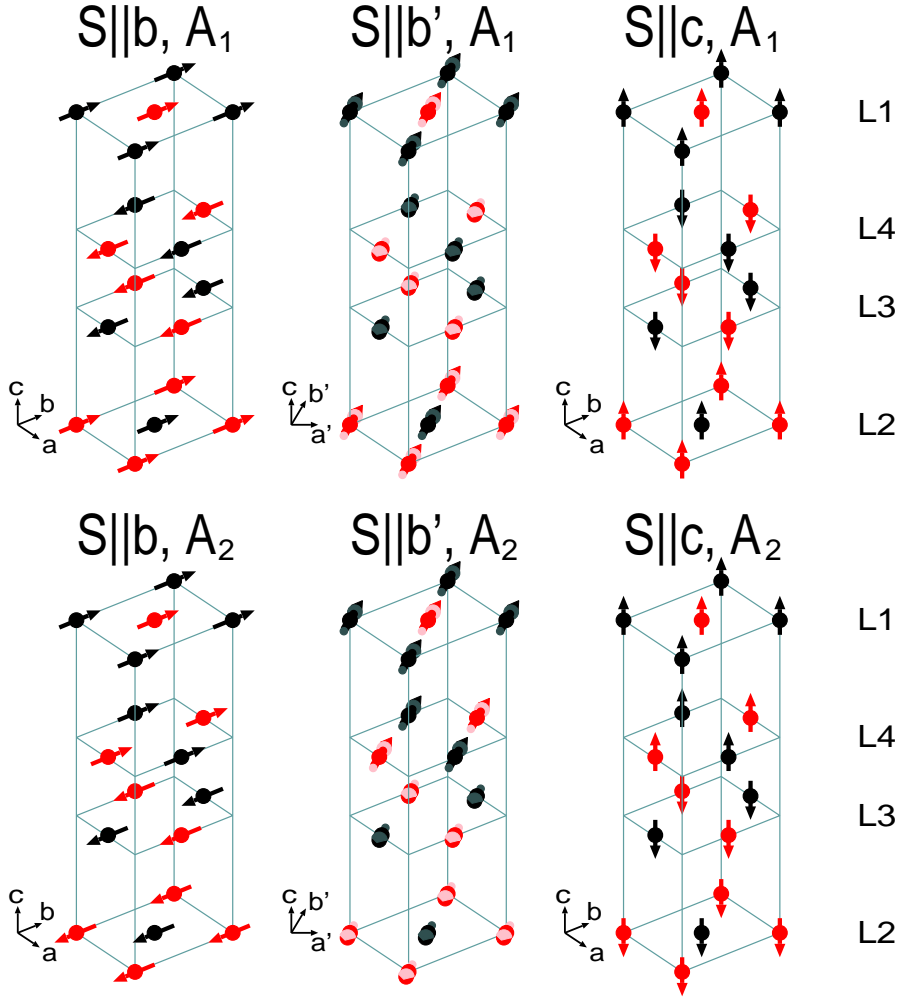


Fig. 6. (Color online) Antiferromagnetic structures obtained in our calculations. The black(red) solid circles represent the Ru site on the A(B) sublattice.

been achieved with the use of Intel Xeon servers at NeRI in AIST.

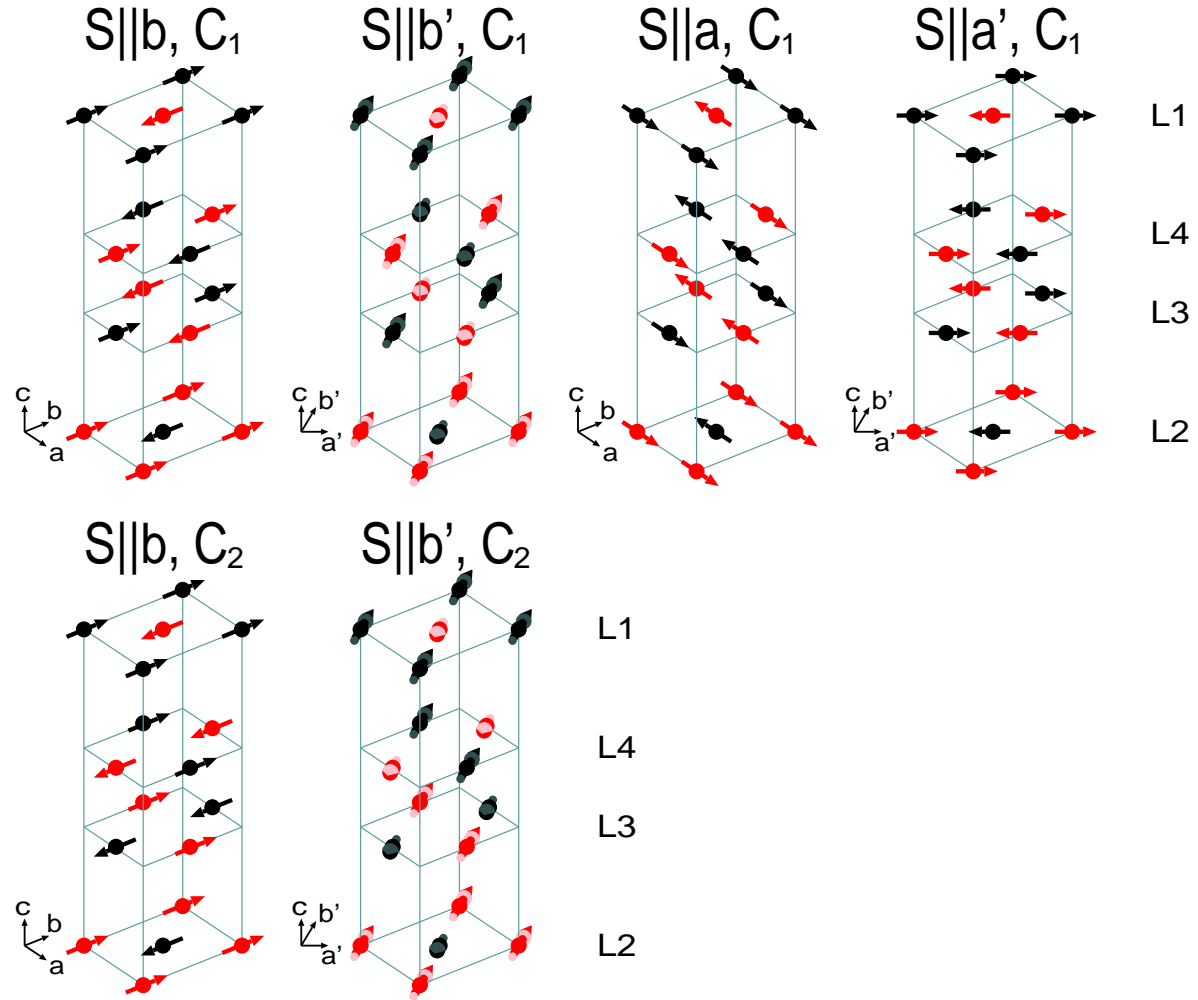


Fig. 7. (Color online) Antiferromagnetic structures obtained in our calculations. The black(red) solid circles represent the Ru site on the A(B) sublattice.

References

- 1) S. A. Grigera, R. S. Perry, A. J. Schofield, M. Chiao, S. R. Julian, G. G. Lonzarich, S. I. Ikeda, Y. Maeno, A. J. Millis and A. P. Mackenzie: *Science* **294** (2001) 329.
- 2) G. Cao, S. McCall and J. E. Crow: *Phys. Rev. B* **55** (1997) R672.
- 3) E. Ohmichi, Y. Yoshida, S. I. Ikeda, N. V. Mushunikov, T. Goto and T. Osada: *Phys. Rev. B* **67** (2003) 024432.
- 4) S.-I. Ikeda, Y. Maeno, S. Nakatsuji, M. Kosaka and Y. Uwatoko: *Phys. Rev. B* **62** (2000) R6089.
- 5) A. V. Puchkov, Z.-X. Shen and G. Cao: *Phys. Rev. B* **58** (1998) 6671.
- 6) Q. Huang, J. W. Lynn, R. W. Erwin, J. Jarupatrakorn and R. J. Cava: *Phys. Rev. B* **58** (1998) 8515.
- 7) L. Capogna, E. M. Forgan, S. M. Hayden, A. Wildes, J. A. Duffy, A. P. Mackenzie, R. S. Perry, S. Ikeda, Y. Maeno, and S. P. Brown: *Phys. Rev. B* **67** (2003) 012504.
- 8) S.-I. Ikeda, N. Shirakawa, S. Koiwai, A. Uchida, M. Kosaka and Y. Uwatoko: *Physica C* **364-365** (2001) 376.
- 9) S.-I. Ikeda, N. Shirakawa, T. Yanagisawa, Y. Yoshida, S. Koikegami, S. Koike, M. Kosaka and Y. Uwatoko: *J. Phys. Soc. Jpn.* **73** (2004) 1322.
- 10) H. Shaked, J. D. Jorgensen, S. Short, O. Chmaissem, S.-I. Ikeda and Y. Maeno: *Phys. Rev. B* **62** (2000) 8725.
- 11) R. Matzdorf, Z. Fang, Ismail, Jiandi Zhang, T. Kimura, Y. Tokura, K. Terakura and E. W. Plummer: *Science* **289** (2000) 746.
- 12) G. Cao, S. McCall, J. E. Crow and R. P. Guertin: *Phys. Rev. Lett.* **78** (1997) 1751.
- 13) H. L. Liu, S. Yoon, S. L. Cooper, G. Cao and J. E. Crow: *Phys. Rev. B* **60** (1999) R6980.
- 14) G. Cao, L. Balicas, Y. Xin, E. Dagotto, J. E. Crow, C. S. Nelson and D. F. Agterberg: *Phys. Rev. B* **67** (2003) 060406.
- 15) G. Cao, L. Balicas, Y. Xin, J. E. Crow and C. S. Nelson: *Phys. Rev. B* **67** (2003) 184405.
- 16) Y. Yoshida, I. Nagai, S.-I. Ikeda, N. Shirakawa, M. Kosaka and N. Môri: *Phys. Rev. B* **69** (2004) 220411.
- 17) J. S. Lee, Y. S. Lee, T. W. Noh, S. Nakatsuji, H. Fukazawa, R. S. Perry, Y. Maeno, Y. Yoshida, S. I. Ikeda, Jaeyun Yu and C. B. Eom: *Phys. Rev. B* **70** (2004) 085103.
- 18) E. Ohmichi, Y. Yoshida, S. I. Ikeda, N. Shirakawa and T. Osada: *Phys. Rev. B* **70** (2004) 104414.
- 19) N. Kikugawa, A. W. Rost, C. W. Hicks, A. J. Schofield and A. P. Mackenzie: *J. Phys. Soc. Jpn.* **79** (2010) 024704.
- 20) Y. Yoshida, S.-I. Ikeda, H. Matsuhata, N. Shirakawa, C. H. Lee and S. Katano: *Phys. Rev. B* **72** (2005) 054412.
- 21) B. Bohnenbuck, I. Zegkinoglou, J. Stremper, C. Schüßler-Langeheine, C. S. Nelson, Ph. Leininger, H.-H. Wu, E. Schierle, J. C. Lang, G. Srajer, S. I. Ikeda, Y. Yoshida, K. Iwata, S. Katano, N. Kikugawa and B. Keimer: *Phys. Rev. B* **77** (2008) 224412.
- 22) W. Bao, Z. Q. Mao, Z. Qu and J. W. Lynn: *Phys. Rev. Lett.* **100** (2008) 247203.
- 23) Y. Yoshida, S.-I. Ikeda, N. Shirakawa, M. Hedo and Y. Uwatoko: *J. Phys. Soc. Jpn.* **77** (2008) 093702.
- 24) G. Cao, S. McCall, J. E. Crow and R. P. Guertin: *Phys. Rev. B* **56** (1997) 5387.
- 25) S. Ikeda, Y. Maeno and T. Fujita: *Phys. Rev. B* **57** (1998) 978.

- 26) A. V. Puchkov, M. C. Schabel, D. N. Basov, T. Startseva, G. Cao, T. Timusk and Z.-X. Shen: Phys. Rev. Lett. **81** (1998) 2747.
- 27) Z. Qu, L. Spinu, H. Q. Yuan, V. Dobrosavljevic, W. Bao, J. W. Lynn, M. Nicklas, J. Peng, T. J. Liu, D. Fobes, E. Flesch and Z. Q. Mao: Phys. Rev. B **78** (2008) 180407.
- 28) K. Iwata, Y. Yoshida, M. Kosaka and S. Katano: J. Phys. Soc. Jpn. **77** (2008) 104716; J. Phys.: Conf. Ser. **150** (2009) 042077.
- 29) Z. Qu, J. Peng, T. J. Liu, D. Fobes, L. Spinu and Z. Q. Mao: Phys. Rev. B **80** (2009) 115130.
- 30) J. Peng, Z. Qu, B. Qian, D. Fobes, T. J. Liu, X. S. Wu, H. M. Pham, L. Spinu and Z. Q. Mao: Phys. Rev. B **82** (2010) 024417.
- 31) I. Hase and Y. Nishihara: J. Phys. Soc. Jpn. **66** (1997) 3517.
- 32) D. J. Singh and I. I. Mazin: Phys. Rev. B **63** (2001) 165101.
- 33) D. J. Singh and S. Auluck: Phys. Rev. Lett. **96** (2006) 097203.
- 34) H.-Y. Kee and Y. B. Kim: Phys. Rev. B **71** (2005) 184402.
- 35) C. Puetter, H. Doh, and H.-Y. Kee: Phys. Rev. B **76** (2007) 235112.
- 36) C. M. Puetter, J. G. Rau, and H.-Y. Kee: Phys. Rev. B **81** (2010) 081105(R).
- 37) S. Raghu, A. Paramakanti, E. A. Kim, R. A. Borzi, S. A. Grigera, A. P. Mackenzie, and S. A. Kivelson: Phys. Rev. B **79** (2009) 214402.
- 38) W.-C. Lee and C. Wu: Phys. Rev. B **80** (2009) 104438; Phys. Rev. Lett. **103** (2009) 176101.
- 39) W.-C. Lee, D. P. Arovas and C. Wu: Phys. Rev. B **81** (2010) 184403.
- 40) M. H. Fischer and M. Sigrist: Phys. Rev. B **81** (2010) 064435.
- 41) F. Forte, M. Cucco, and C. Noce: Phys. Rev. B **82** (2010) 155104.
- 42) T. Nomura and K. Yamada: J. Phys. Soc. Jpn. **69** (2000) 1856.
- 43) T. Hotta and E. Dagotto: Phys. Rev. Lett. **88** (2001) 017201.
- 44) I. Eremin, D. Manske, and K. H. Bennemann: Phys. Rev. B **65** (2002) 220502(R).
- 45) M. Kurokawa and T. Mizokawa: Phys. Rev. B **66** (2002) 024434.
- 46) T. Mizokawa, L. H. Tjeng, H.-J. Lin, C. T. Chen, S. Schuppler, S. Nakatsuji, H. Fukazawa, and Y. Maeno: Phys. Rev. B **69** (2004) 132410.
- 47) S. Okamoto and A. J. Millis: Phys. Rev. B **70** (2004) 195120.
- 48) T. Oguchi: J. Phys. Soc. Jpn. **78** (2009) 044702.
- 49) T. Kita, T. Ohashi, and S.-i. Suga: Phys. Rev. B **79** (2009) 245128.
- 50) S. Nakatsuji and Y. Maeno: Phys. Rev. Lett. **84** (2000) 2666.
- 51) X. Ke, T. Hong, J. Peng, S. E. Nagler, G. E. Granroth, M. D. Lumsden, and Z. Q. Mao: Phys. Rev. B **84** (2011) 014422.
- 52) C. Stingl, R. S. Perry, Y. Maeno, and P. Gegenwart: Phys. Rev. Lett. **107** (2011) 026404.